

Alma Mater Studiorum Università di Bologna
Archivio istituzionale della ricerca

Infrared and Raman spectroscopic features of clinocllore $\text{Mg}_6\text{Si}_4\text{O}_{10}(\text{OH})_8$: A density functional theory contribution

This is the final peer-reviewed author's accepted manuscript (postprint) of the following publication:

Published Version:

Ulian G., Moro D., Valdrè Giovanni (2020). Infrared and Raman spectroscopic features of clinocllore $\text{Mg}_6\text{Si}_4\text{O}_{10}(\text{OH})_8$: A density functional theory contribution. APPLIED CLAY SCIENCE, 197, 1-11 [10.1016/j.clay.2020.105779].

Availability:

This version is available at: <https://hdl.handle.net/11585/782000> since: 2024-02-13

Published:

DOI: <http://doi.org/10.1016/j.clay.2020.105779>

Terms of use:

Some rights reserved. The terms and conditions for the reuse of this version of the manuscript are specified in the publishing policy. For all terms of use and more information see the publisher's website.

This item was downloaded from IRIS Università di Bologna (<https://cris.unibo.it/>).
When citing, please refer to the published version.

(Article begins on next page)

Infrared and Raman spectroscopic features of Clinochlore

Mg₆Si₄O₁₀(OH)₈: a Density Functional Theory contribution

Gianfranco Ulian, Daniele Moro and Giovanni Valdrè*

Centro di Ricerca Interdisciplinare di Biomineralogia, Cristallografia e Biomateriali

Dipartimento di Scienze Biologiche, Geologiche e Ambientali - Università di Bologna

Piazza di Porta San Donato 1, 40126 Bologna, Italy

**E-mail: giovanni.valdre@unibo.it*

Abstract

Mineral identification and analysis are often performed by using vibrational spectroscopies, namely infrared and Raman techniques. However, very few spectroscopy data are available on clinochlore, an important phyllosilicate with manifold applications in several fields. In the present work, *ab initio* Density Functional Theory simulation was employed to calculate the infrared and Raman spectra at Γ points and the phonon dispersion at different \mathbf{k} -points of the magnesium end-member of clinochlore, with ideal chemical formula Mg₆Si₄O₁₀(OH)₈ and space group *C2/m*. Each phonon mode of the mineral was assigned to specific vibrations of the ionic groups in the structure. The theoretical results were found in good agreement with the available experimental data in literature, further extending the knowledge on the vibrational properties of clinochlore, which could be useful for experimental characterization of this mineral phase in various and different fields of research.

Keywords: Clinochlore, infrared and Raman spectroscopies, phonon dispersion relations, Density Functional Theory

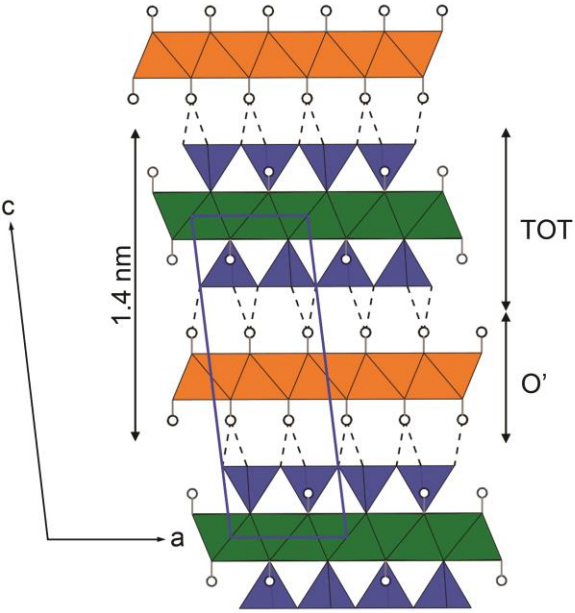
23 1. Introduction

24 Clinochlore is a phyllosilicate mineral of the chlorite group whose ideal formula is
25 $\text{Mg}_3^{\text{IV}}\text{Mg}_3^{\text{VI}}\text{Si}_4^{\text{IV}}\text{O}_{10}(\text{OH})_8$, composed by alternately stacked brucite-like (labelled as O') and talc-like
26 (2:1 or TOT) layers (see Figure 1) held together by hydrogen bonds. According to conventional
27 mineralogical rules, the superscripts VI', VI, and IV refer to six-fold coordination of the octahedral
28 interlayer cation, six-fold coordination of the TOT layer octahedral cation and the four-fold coordination
29 of the tetrahedral cation, respectively (Bayliss, 1975; Wiewiora, 1990).

30 Clinochlore is an interesting clay mineral due to its peculiar surface properties. In fact, when cleaved,
31 its surface often presents remainders of the O' layer above an intact TOT layer, resulting in a
32 simultaneous exposition of regions related to the two layers. According to previous atomic force
33 microscopy, Kelvin-probe force microscopy studies and quantum-mechanical simulations (Valdrè et al.,
34 2011c; Valdrè et al., 2012; Moro et al., 2016; Moro et al., 2019a), the brucite-like layer is hydrophobic,
35 whereas the 2:1 layer is hydrophilic, hence they present different features as adsorbents and/or catalysts.
36 To cite some example, chlorite is able to adsorb, organize and self-assemble nucleotides, RNA and DNA
37 (Valdrè, 2007; Valdrè et al., 2011a; Valdrè et al., 2011b), and amino acids, *e.g.* glycine and L-alanine
38 (Moro et al., 2015; Moro et al., 2019b). The cited biomolecules were found selectively adsorbed on the
39 brucite-like sheet and atomic force microscopy revealed different molecular conformations at the mineral
40 surface. For example, RNA filaments adsorbed on atomic flat terraces were found as globular structures,
41 whereas they were linearized on the edges of the brucite-like sheet (Valdrè et al., 2011b). DNA molecules
42 were mainly found on the edges of the $\text{Mg}(\text{OH})_6$ zones both in network-like and linear conformations
43 and, in some cases, also as “bridges” between two parallel brucite-like stripes. In the case of amino acids,
44 they were experimentally found as dot-like structures (single molecules), agglomerates and filament-like
45 structures (Moro et al., 2015; Moro et al., 2019b). Very high adsorption energy between single molecules

46 and the brucite-like sheet was calculated from *ab initio* simulations, whose value was in the range 77 –
 47 82 kJ/mol for glycine and 110 – 280 kJ/mol for L-alanine, depending on the local crystal-chemistry. The
 48 positive sign here indicates the energy necessary to desorb the molecule from the surface.

49 In addition zeolitic-type Brønsted-Lowry sites, which are known to control catalytic processes, were
 50 discovered on atomic flat surfaces (bi-dimensional systems) in chlorites and modelled by *ab initio*
 51 techniques (Valdrè et al., 2011c). For these reasons, there are many and various important applications
 52 of clinochlore (and clay minerals, in general) in several fields, from petrochemical refining, fine-
 53 chemical production, to water and air purification (Phuakkong et al., 2011; Stueckenschneider et al.,
 54 2014).



55
 56 **Figure 1.** View along the **b**-axis of an ideal clinochlore mineral structure (s.g. *C2/m*). Talc-like (2:1,
 57 TOT) and brucite-like (O') structural units are indicated. Blue tetrahedrons represent the SiO₄, whereas
 58 orange and green octahedrons represent MgO₆ groups in the O' and TOT units, respectively. The blue
 59 solid line shows the crystallographic unit cell, whereas the dashed lines indicate the hydrogen bonds
 60 between the structural units.

61 One of the leading and simplest methods to investigate bulk structures and/or processes occurring at
62 the surface is vibrational (infrared, IR or Raman) spectroscopy. For example, IR/Raman experiments are
63 employed to recognize the presence of a mineral phase, by comparing the acquired spectrum with those
64 available in databases (Fries and Steele, 2018), or to study fluid inclusions in minerals (Rosso and
65 Bodnar, 1995). For surface processes, Attenuated Total Reflectance – Fourier Transform Infrared (ATR-
66 FTIR) and confocal Raman spectroscopy are useful tools to investigate surfaces and reactions between
67 minerals and the environment (*e.g.* molecules of gas/liquid) or intra-phase processes (King and Geisler,
68 2018). Very recently, infrared and Raman spectroscopy at the nanoscale, *i.e.* nano-FTIR, near-field FTIR
69 and tip-enhanced Raman spectroscopy (TERS), are leading for promising applications and researches at
70 the sub-micrometre level with very high resolution (Dominguez et al., 2014; Firkala et al., 2018;
71 Bhattarai and El-Khoury, 2019; Kumar et al., 2019). The common factor between different applications
72 is that a detailed knowledge of the vibrational modes of the mineral phase is required. For clinocllore,
73 very few data on the infrared and Raman properties are available in literature (Gopal et al., 2004;
74 Lafuente et al., 2016). In addition, the interpretation of experimental spectra is often difficult for several
75 reasons, such as (1) the presence of impurities in both natural and synthetic samples, (2) the morphology
76 of the samples (3) the presence of overtones and/or combination bands; (4) the impossibility to observe
77 modes associated with weak intensities (low transition moments), (5) the availability only of poor
78 crystalline samples, resulting in band broadening with extensive overlap of the signals, (6) polarization
79 anisotropy in nano-FTIR and Raman and (7) residual strains in the minerals. In this perspective, *ab initio*
80 quantum-mechanical simulations represent an effective tool to overcome the issues mentioned above,
81 because they allow for the calculation of the phonon modes of solids. From the analysis of the vibrational
82 motion of the atoms in the unit cell, it is also possible to successfully identify and assign to specific
83 normal modes all of the fundamental vibrational transitions of the system in consideration, a task that is
84 still very difficult by experimental means.

In the present work, a fundamental and detailed theoretical analysis of the infrared and Raman responses of monoclinic clinochlore ($C2/m$ space group) is provided to fill the knowledge gap on this important clay mineral phase. The chemical composition here considered is that of an ideal, clinochlore end-member, where every T and M sites are occupied by silicon and magnesium, respectively. This monoclinic clinochlore model was geometrically optimized and its vibrational features at Γ point were investigated in detail using Density Functional Theory. Finally, the theoretical phonon dispersion relations of this mineral phase is reported and compared with the few data reported by Collins et al. (1993) on the acoustic phonons.

2. Theoretical methods

All the simulations related to the geometry optimization and the calculation of the phonon properties of clinochlore were performed within the Density Functional Theory (DFT) framework using the CRYSTAL17 periodic code (Dovesi et al., 2018), whereas graphical representations were carried out with the molecular graphics program VESTA (Momma and Izumi, 2011) and Moldraw (Ugliengo et al., 1993).

The chosen Hamiltonian was the hybrid B3LYP (Lee et al., 1988; Becke, 1993), where 20% of Hartree-Fock energy contributes to the DFT exchange term, because of its suitability for the *ab initio* investigations of vibrational properties of both molecular and solid (periodic) systems (Pascale et al., 2004; Pascale et al., 2005). The total energy (exchange/correlation) was evaluated on a pruned grid with 75 radial points and 974 angular points, subdivided in 5 intervals of 86, 194, 350, 974 and 350 points according to the Gauss-Legendre quadrature and Lebedev schemes (Prencipe et al., 2004). The thresholds controlling the accuracy of the calculation of the Coulomb and exchange integrals have been set to 10^{-8} (ITOL1 to ITOL4) and 10^{-16} (ITOL5); this means that when the overlap between two atomic orbitals is

108 lower than $10^{-\text{ITOL}}$, the corresponding integral is either discarded or treated with less precision, as
109 explained by Dovesi et al. (2018). The Hamiltonian matrix has been diagonalized through the Monkhorst
110 and Pack scheme (Monkhorst and Pack, 1976), using a $6 \times 6 \times 2$ k-mesh, which leads to 26 reciprocal lattice
111 points (**k**-points). Weak intermolecular interactions, such as van der Waals forces, play a relevant role in
112 determining the internal geometries of the crystal and its related properties. For this reason, a modified
113 DFT-D2 scheme proposed by Grimme (2006) was employed to include those energy contributions to the
114 final energy (Civalleri et al., 2008).

115 Within the Linear Combination of Atomic Orbitals (LCAO) approach, atomic and crystalline orbitals
116 have been described by Gaussian-type orbitals basis sets. In particular, for magnesium and oxygen a 8-
117 511d1G and a 8-411d11G (Valenzano et al., 2006; Ulian et al., 2016, 2018) basis sets were employed,
118 respectively. Silicon and hydrogen were described by a 88-31G* (Nada et al., 1996; Ulian and Valdrè,
119 2015; Ulian et al., 2018) and a 3-1p1G basis sets (Gatti et al., 1994; Moro et al., 2015; Ulian et al., 2018),
120 respectively. The chosen basis sets are well balanced, allowing accurate calculations in both molecular
121 and crystal structures with sustainable computational costs.

122 The geometry of monoclinic clinocllore $\text{Mg}_6\text{Si}_4\text{O}_{10}(\text{OH})_{10}$ (space group *C2/m*) was taken from the
123 experimental refining of Welch and Marshall (2001) on a synthetic sample, which represents the closest
124 structure to start with. All the simulations on this model were performed on the primitive cell, but
125 structural results are referred to the crystallographic cell to ease the comparison (*vide infra*).

126 The cell parameters and internal coordinates of each model were optimized using the analytical
127 gradient method for the atomic positions and a numerical gradient for the unit-cell parameters, to find
128 the equilibrium geometry. The self-consistent field (SCF) procedure for the total energy calculations was
129 considered converged when the energy difference between the last step and the previous one was less
130 than 10^{-8} Ha during geometry optimization. The convergence on the structural optimization was reached
131 when each component of the gradient was smaller than $3 \cdot 10^{-5}$ hartree bohr⁻¹ and displacements with

respect to the previous step were smaller than $12 \cdot 10^{-5}$ bohr. The Hessian matrix was upgraded with the Broyden-Fletcher-Goldfarb-Shanno (BFGS) algorithm. The structure parameters and atomic coordinates of the optimized clinocllore model (crystallographic cell) are reported in Table 1.

Table 1. Crystallographic cell structure (lattice parameters and atomic positions) of monoclinic stoichiometric clinocllore (s.g. $C2/m$), optimized at the Density Functional Theory/B3LYP-D* level, compared to experimental results.

B3LYP-D*					Experimental (Welch and Marshall, 2001)				
<i>a</i>	<i>b</i>	<i>c</i>	β	<i>V</i>	<i>a</i>	<i>b</i>	<i>c</i>	β	<i>V</i>
5.3297	9.2309	14.8947	96.829	727.590	5.332	9.224	14.414	97.07	703.52
Internal geometry					Internal geometry				
<i>Atom</i>	<i>x/a</i>	<i>y/b</i>	<i>z/c</i>	<i>Wyckoff</i>	<i>Atom</i>	<i>x/a</i>	<i>y/b</i>	<i>z/c</i>	<i>Wyckoff</i>
H1	0.2130	0.5000	0.1364	4i	H1	0.200	0.500	0.142	4i
H2	0.6204	0.5000	0.3639	4i	H2	0.117	0.320	0.358	4i
H3	0.1220	0.3338	0.3641	8j	H3	0.120	0.000	0.371	8j
Mg1	0.0000	0.0000	0.0000	2a	Mg1	0.000	0.000	0.000	2a
Mg2	0.5000	0.1663	0.0000	4g	Mg2	0.000	0.160	0.500	4g
Mg3	0.0000	0.3337	0.0000	4h	Mg3	0.000	0.353	0.000	4h
Mg4	0.0000	0.5000	0.5000	2d	Al4*	0.000	0.500	0.500	2d
O(a)	0.1910	0.1668	0.0739	8j	O1	0.185	0.172	0.080	8j
O(b)1	0.2136	0.0000	0.2209	4i	O2	0.228	0.000	0.234	4i
O(b)2	0.5029	0.2369	0.2210	8j	O3	0.509	0.220	0.231	8j
O(h)1	0.1907	0.5000	0.0715	4i	O4	0.181	0.500	0.068	4i
O(h)2	0.1424	0.0000	0.4283	4i	O5	0.168	0.000	0.435	4i
O(h)3	0.1432	0.3336	0.4285	8j	O6	0.135	0.337	0.430	8j
Si1	0.2277	0.1667	0.1844	8j	Si1 [†]	0.224	0.166	0.193	8j

Notes: The experimental sample contained an Al-substitution in the O' layer (Al4 atom, marked with an asterisk) corresponding to the Mg4 atom in the simulated stoichiometric model and a partial substitution (25%) of silicon (Si1, marked with †) with aluminium.

There is an overall good agreement between the theoretical and experimental results of Welch and Marshall (2001), with the main difference residing in the *c*-axis length. Indeed, the synthetic Mg-rich clinocllore refined in the $C2/m$ space group presented a chemical formula $(\text{Mg}_2\text{Al})^{\text{IV}}\text{Mg}_3^{\text{VI}}(\text{AlSi}_3)^{\text{IV}}\text{O}_{10}(\text{OH})_8$, characterized by the following cation occupation: $T = 0.25\text{Al} + 0.75\text{Si}$, $M1 = M2 = M3 = \text{Mg}$, $M4 = \text{Al}$, whereas the simulated model has chemical composition $(\text{Mg}_3)^{\text{IV}}\text{Mg}_3^{\text{VI}}(\text{Si}_4)^{\text{IV}}\text{O}_{10}(\text{OH})_8$. The presence of some fraction of aluminium substitutions in both the tetrahedral sheet of the TOT layer and the O' layer increases the Coulomb (ionic) interactions between them, resulting in a lowered TOT – O' distance.

145 Harmonic phonon modes and vibrational frequencies were calculated at the Γ point on the optimized model of
146 monoclinic clinochlore by diagonalizing the mass-weighted Hessian matrix (dynamical matrix), whose elements
147 are the second derivatives of the lattice potential with respect to mass-weighted atomic displacements (Pascale et
148 al., 2004). For these calculations, strict threshold criteria (10^{-10} Ha) were applied for the energy convergence to
149 improve the accuracy of the vibrational results. Also, an anharmonic correction for OH stretching modes was
150 applied, following the procedure described by Tosoni and co-workers (2005).

151

152 **3. Results and discussion**

153 Monoclinic, stoichiometric clinochlore $\text{Mg}_3(\text{OH})_6\text{Mg}_3\text{Si}_4\text{O}_{10}(\text{OH})_2$ (space group $C2/m$, point group
154 C_{2h}) has a single unit formula per primitive unit cell (36 atoms). The phonon modes of this mineral phase
155 are then $36 \times 3 = 108$, subdivided in three modes related to acoustic phonons (translations of the whole
156 lattice) and 105 to optical ones. The presence of an inversion centre in the mineral leads to (1) vibrational
157 modes active only in infrared or in Raman, but not in both (mutual exclusion rule), (2) the subdivision
158 of the modes in *gerade* (labelled as *g*) and *ungerade* (*u*), namely vibrations that are symmetric or
159 antisymmetric with respect to the inversion centre, respectively and (3) the absence of the longitudinal
160 optical (LO) - transverse optical (TO) splitting. The LO-TO splitting is common in many layered
161 silicates, in which atoms that vibrates perpendicularly to the layers (the so-called polar modes, or Fröhlich
162 modes) should vibrate at their longitudinal optical frequency (Balan et al., 2001; Prencipe et al., 2009);
163 however, the presence of the inversion centre nullify this effect (Prencipe et al., 2009).

164 The Γ -point vibrational modes can be classified according to the irreducible representation of the C_{2h}
165 point group of the mineral as $\Gamma_{\text{total}} = \Gamma_{\text{acoustic}} + \Gamma_{\text{optic}} = 27A_g + 24A_u + 24 B_g + 33A_u$ (Kroumova et al.,
166 2003). The A_u and B_u modes are active in infrared spectroscopy, whereas A_g and B_g ones are Raman
167 active. The three acoustic phonons are given by $A_u + 2B_u$ modes. A site symmetry analysis according to

168 Kroumova et al. (2003) is reported in Table 2. Each atom contributes to all active vibrational modes,
 169 Mg1 and Mg4 atoms in the trioctahedral sheet of the talc-like layer and of the brucite-like layer,
 170 respectively, are not associated with any *gerade* mode, which are those active in Raman spectroscopy.

Table 2. Site symmetry analysis for monoclinic clinocllore (s.g. $C2/m$).

<i>Atom</i>	<i>Layer</i>	<i>Wyckoff</i>	<i>Symmetry</i>
H1	TOT	4i	$2A_g + A_u + B_g + 2B_u$
H2	O'	4i	$2A_g + A_u + B_g + 2B_u$
H3	O'	8j	$3A_g + 3A_u + 3B_g + 3B_u$
Mg1	TOT	2a	$A_u + 2B_u$
Mg2	TOT	4g	$A_g + A_u + 2B_g + 2B_u$
Mg3	O'	4h	$A_g + A_u + 2B_g + 2B_u$
Mg4	O'	2d	$A_u + 2B_u$
O(a)	TOT	8j	$3A_g + 3A_u + 3B_g + 3B_u$
O(b)1	TOT	4i	$2A_g + A_u + B_g + 2B_u$
O(b)2	TOT	8j	$3A_g + 3A_u + 3B_g + 3B_u$
O(h)1	TOT	4i	$2A_g + A_u + B_g + 2B_u$
O(h)2	O'	4i	$2A_g + A_u + B_g + 2B_u$
O(h)3	O'	8j	$3A_g + 3A_u + 3B_g + 3B_u$
Si1	TOT	8j	$3A_g + 3A_u + 3B_g + 3B_u$
Total			$27A_g + 24A_u + 24B_g + 33B_u$

171

172 In Table 3, the calculated Γ -point frequencies of the transverse optical vibrational modes of monoclinic
 173 clinocllore, together with their transition moment corresponding to infrared and Raman activity are
 174 reported. The infrared spectrum of clinocllore was analytically calculated using the classical absorption
 175 formula as explained by Maschio et al. (2012):

176
$$A(\nu) = \frac{1}{3} \sum_{ii=1}^3 \frac{4\pi}{\lambda \rho} \text{Im}[n_{ii}(\nu)]$$

177 where $A(\nu)$ is the infrared absorption, λ if the wavelength of the incident light, ρ is the density of the
 178 mineral, n is the complex refractive index and ii represents the polarization direction. The real and
 179 imaginary parts of the refractive index n_{ii} were calculated as:

180
$$\left\{ \text{Re}[n_{ii}(\nu)] \right\}^2 - \left\{ \text{Im}[n_{ii}(\nu)] \right\}^2 = \text{Re}[\varepsilon_{ii}(\nu)]$$

$$2 \operatorname{Re}[n_{ii}(\nu)] \cdot \operatorname{Im}[n_{ii}(\nu)] = \operatorname{Im}[\varepsilon_{ii}(\nu)]$$

where $\varepsilon_{ii}(\nu)$ is the complex dielectric tensor, computed for each inequivalent polarization direction according to a classical Drude-Lorentz model:

$$\varepsilon_{ii}(\nu) = \varepsilon_{\infty,ii} + \sum_p \frac{f_{p,ii} \nu_p^2}{\nu_p^2 - \nu^2 - i\nu\gamma_p}.$$

In the previous equation, ε_{∞} indicates the optical dielectric tensor, which was calculated using a couple-perturbed Kohn-Sham approach (Ferrero et al., 2008a; Ferrero et al., 2008b), whereas ν_p, f_p and γ_p are the transverse optical frequency, oscillator strength and damping factor of the p^{th} vibrational mode, respectively. The damping factor represents the full width at half maximum of each vibrational mode and was set to 8, which is a value that provides band broadening similar to that of experimental samples and also the default employed by CRYSTAL, as described by Maschio and co-workers (2012).

For what regards the Raman spectrum of clinocllore, it was calculated for a polycrystalline powder by using the transverse optical vibrational modes by means of a pseudo-Voigt functional form (Maschio et al., 2013a, b):

$$A(\nu) = \eta L(\nu) + (1 - \eta) G(\nu)$$

where, in this case, $A(\nu)$ represents the Raman intensity and $L(\nu)$ and $G(\nu)$ are given by:

$$L(\nu) = \sum_p \frac{I_p}{\pi} \frac{\gamma_p/2}{(\nu - \nu_p)^2 + (\gamma_p/2)^2}$$

$$G(\nu) = \sum_p 2\sqrt{\frac{\ln 2}{\pi}} \frac{I_p}{\gamma_p} \exp\left[-\frac{4\ln 2(\nu - \nu_p)^2}{\gamma_p^2}\right]$$

198 with I_p the computed Raman intensities for the p^{th} vibrational mode and η is the Lorentz factor. A pure
199 Lorentzian form, which is the default of CRYSTAL (Maschio et al., 2013a), corresponding to $\eta = 1$, was
200 employed to obtain the typical sharp peaks of Raman spectra (Dovesi et al., 2018). The infrared and
201 Raman spectra for monoclinic clinocllore calculated as described above are reported in Figure 2a and
202 Figure 2b, respectively.

203

204

Table 3. Phonon frequencies (ν) and their irreducible representation (IRREP) of monoclinic clinocllore $\text{Mg}_3(\text{OH})_6\text{Mg}_3\text{Si}_4\text{O}_{10}(\text{OH})_2$ (s.g. C2/m) as obtained from Density Functional Theory simulations at the B3LYP-D* level. Amplitude is referred to transition moments in infrared (Ampl. IR) and Raman (Ampl. R).

Mode	ν (cm^{-1})	IRREP	Ampl. IR	Ampl. R	Mode	ν (cm^{-1})	IRREP	Ampl. IR	Ampl. R
1	0	B _u	0.0	0.0	55	450	A _u	596.0	0.0
2	0	B _u	0.0	0.0	56	454	B _u	1404.5	0.0
3	0	A _u	0.0	0.0	57	458	B _g	0.0	56.4
4	22	B _u	1.8	0.0	58	458	A _g	0.0	55.4
5	25	A _u	2.3	0.0	59	460	B _g	0.0	13.3
6	82	B _u	0.2	0.0	60	472	A _u	712.3	0.0
7	106	B _u	3.5	0.0	61	476	A _g	0.0	4.0
8	106	A _g	0.0	58.2	62	476	B _u	16.7	0.0
9	112	B _g	0.0	17.4	63	479	B _g	0.0	2.7
10	114	A _g	0.0	20.1	64	479	A _u	24.1	0.0
11	158	B _u	2.8	0.0	65	481	A _g	0.0	23.5
12	159	B _g	0.0	4.2	66	483	A _g	0.0	75.2
13	179	B _u	4.6	0.0	67	502	B _u	662.7	0.0
14	185	A _u	2.9	0.0	68	519	B _g	0.0	2.3
15	200	A _g	0.0	191.0	69	527	B _u	371.9	0.0
16	245	B _g	0.0	2.6	70	529	A _u	4.2	0.0
17	245	B _u	1.0	0.0	71	531	A _g	0.0	2.5
18	273	B _u	22.4	0.0	72	615	B _u	199.5	0.0
19	285	B _g	0.0	7.8	73	619	A _g	0.0	29.3
20	287	A _g	0.0	7.5	74	628	B _u	264.0	0.0
21	294	A _g	0.0	15.6	75	629	A _u	0.7	0.0
22	298	A _u	0.0	0.0	76	630	A _g	0.0	5.5
23	306	B _u	11.1	0.0	77	631	B _u	4.0	0.0
24	307	B _g	0.0	0.4	78	631	B _g	0.0	3.2
25	312	A _u	0.7	0.0	79	635	B _g	0.0	2.2
26	313	A _g	0.0	6.8	80	636	A _u	0.6	0.0
27	314	B _g	0.0	2.5	81	688	A _g	0.0	298.7
28	329	B _u	7.9	0.0	82	709	B _u	17.7	0.0
29	334	A _g	0.0	6.2	83	753	B _u	351.3	0.0
30	340	B _g	0.0	7.8	84	758	A _u	373.7	0.0
31	353	A _u	12.7	0.0	85	761	B _g	0.0	30.7
32	355	B _g	0.0	0.9	86	763	A _g	0.0	31.4
33	375	A _g	0.0	80.3	87	796	A _g	0.0	12.7
34	375	A _u	1.1	0.0	88	796	B _u	3.8	0.0
35	377	B _u	2.2	0.0	89	797	A _u	2.2	0.0
36	387	A _g	0.0	3.1	90	798	B _g	0.0	13.1
37	387	B _u	7.1	0.0	91	906	B _g	0.0	0.2
38	388	B _g	0.0	1.9	92	907	A _u	2.4	0.0
39	390	A _u	1.8	0.0	93	989	B _u	1945.4	0.0
40	390	B _g	0.0	0.1	94	1013	A _u	2672.1	0.0
41	392	A _g	0.0	11.3	95	1013	B _g	0.0	3.5
42	397	A _u	242.6	0.0	96	1013	B _u	2678.2	0.0
43	398	B _u	140.6	0.0	97	1013	A _g	0.0	3.5
44	400	B _u	515.4	0.0	98	1060	A _g	0.0	27.9
45	400	A _u	656.5	0.0	99	1092	B _g	0.0	0.0
46	403	B _g	0.0	0.4	100	1092	A _u	0.2	0.0
47	407	B _u	380.1	0.0	101†	3697	B _u	130.2	0.0
48	412	A _u	846.9	0.0	102†	3698	A _g	0.0	111.6
49	415	A _g	0.0	2.5	103†	3831	B _g	0.0	2.7
50	426	B _u	1730.2	0.0	104†	3831	A _u	4.9	0.0
51	431	A _u	1215.7	0.0	105†	3832	B _u	10.9	0.0
52	434	B _u	398.3	0.0	106†	3832	A _g	0.0	12.1
53	443	B _g	0.0	11.8	107†	3843	B _u	513.0	0.0
54	448	A _g	0.0	10.2	108†	3844	A _g	0.0	1000.0

Notes: modes 1 – 3 are acoustic phonons. IRREP is the irreproducible representation of the mode. Ampl. IR and Ampl. R are the calculated infrared and Raman transition amplitudes, respectively. Modes labelled with † are corrected for anharmonicity as of the model of Tosoni and co-workers (2005).

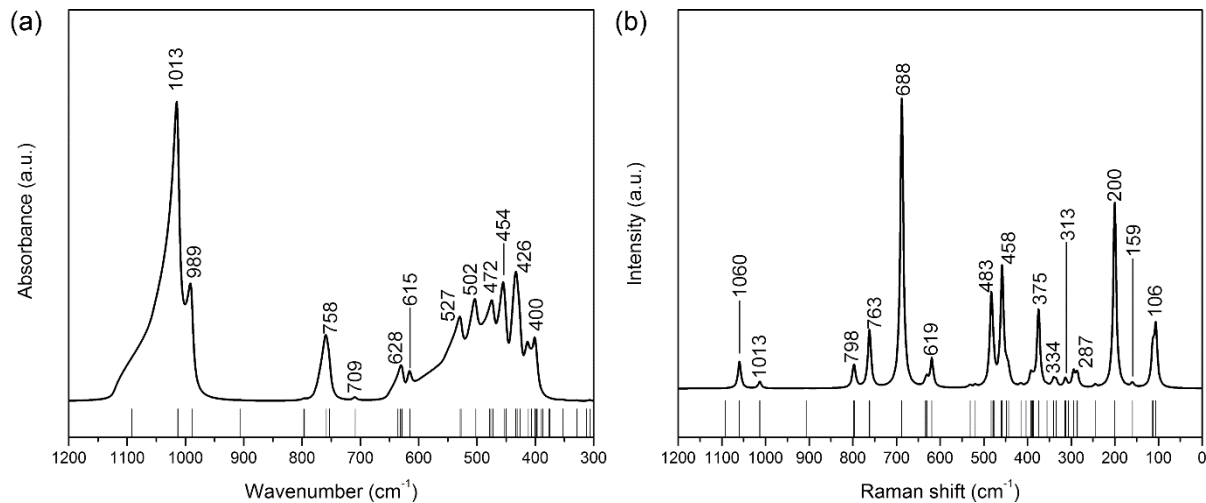


Figure 2. Simulated infrared (a) and Raman (b) spectra of monoclinic clinocllore $\text{Mg}_3(\text{OH})_6\text{Mg}_3\text{Si}_4\text{O}_{10}(\text{OH})_2$ (space group $C2/m$).

Three regions were calculated in both the infrared and Raman spectra: a low-frequency region 0 – 500 cm^{-1} ; an intermediate-frequency region between 500 and 1100 cm^{-1} ; and a high-frequency region up in the 3700 – 4000 cm^{-1} . The assignment of each normal mode was carried out by means of (1) graphical animation of the atom motions using Moldraw (Ugliengo et al., 1993), (2) analysis of the vibrational eigenvectors and of the potential energy distribution (PED), provided by CRYSTAL and (3) isotopic substitutions, in particular $^{25}\text{Mg} \rightarrow ^{24}\text{Mg}$, $^{29}\text{Si} \rightarrow ^{28}\text{Si}$ and $^2\text{D} \rightarrow ^1\text{H}$. CRYSTAL can easily calculate isotopic shifts because the vibrational frequencies and normal modes are obtained from the diagonalization of the mass-weighted dynamical matrix W , which is defined as:

$$W_{\alpha,\beta}(\mathbf{k} = 0) = \frac{H}{\sqrt{M_\alpha M_\beta}}$$

where H is the dynamical matrix (matrix of the second-derivatives of the energy with respect to atom displacements) and M_α and M_β are the masses of the atoms associated to the vibrational motion. Vibrational isotopic shifts related to the $^{25}\text{Mg} \rightarrow ^{24}\text{Mg}$, $^{29}\text{Si} \rightarrow ^{28}\text{Si}$ substitutions are reported in Tables

221 4, whereas Table 5 shows those of the deuterium \rightarrow hydrogen substitution. In the following, the results
222 are discussed in details for the three spectral regions and compared to the available experimental results.

223

224 **3.1. The 0–500 cm^{-1} region**

225 In this region, 64 optic modes were computed, of which 33 are IR active ($14 A_u + 19 B_u$) and 31 are
226 active in Raman ($16 A_g + 15 B_g$). Up to about 400 cm^{-1} , IR modes have very low intensity, which make
227 them very difficult to observe experimentally. Even at theoretical level, the calculated amplitudes are
228 very low. For the sake of an example, the analysis of the potential energy distribution revealed that the
229 B_u mode at 106 cm^{-1} is related to a rotation of the Si – O(b) basal triangle, which is a mode with very
230 low transition dipole moment in IR.

231 Below 400 cm^{-1} , Raman spectroscopy is more informative and sensitive. The weak band at 106 cm^{-1}
232 is again related to the Si – O(b) triangle rotation as noted from IR. Two extremely weak signals were
233 calculated at 112 and 114 cm^{-1} , which were assigned to bending modes of Si_2O_5 layers. The mode at 159
234 cm^{-1} was related, instead, to a combination of the out-of-plane vibration of the magnesium ions and to
235 librations of the OH groups in the brucite-like interlayer. There is a quite intense peak at 200 cm^{-1} related
236 to a symmetric MgO_6 vibration that moves also the T sheets along the *c*-axis direction. These results are
237 in good agreement with the experimental observations of Rinaudo et al. (2004) on phlogopite, where
238 these signals were measured at 102 , 120 , 153 and 195 cm^{-1} . The only exception is the assignment of the
239 mode at 102 cm^{-1} , which the authors correlated to MO_6 vibrations. Three very weak bands were observed
240 at 334 , 313 and 287 cm^{-1} , which were assigned to Si – O(b) – Si bending, Mg – O(h) – Mg bending in
241 the brucite-like layer and Si – O(b) – Si bending, respectively. A weak band at 375 cm^{-1} is related to a
242 Mg – O(h) – Mg bending mode of the TOT layer. Finally, the peaks in the Raman spectrum at 458 cm^{-1}

243 and 483 cm^{-1} are related to two modes of the O' layer, namely OH librations and Mg – O(h) – Mg
244 bending, respectively.

245 Above 400 cm^{-1} , quantum mechanical simulations of the infrared spectrum of clinocllore provided
246 vibrational signals with higher intensities (about 100 times those below 400 cm^{-1}). Between 500 and 600
247 cm^{-1} , the spectrum is mainly due to octahedral MgO_6 modes. The first peak (400 cm^{-1}) is given by two
248 optic modes related to Mg – O(h) – Mg bending mode of the TOT layer, one showing Mg displacement
249 normal to the layer and the second with Mg motion parallel to the (001) plane. There are two strong
250 signals at 426 cm^{-1} and 431 cm^{-1} related to OH librations (Mg – O(h) – H bending) in the O' layer,
251 normal to [001]. An MgO_6 deformation parallel to the (001) plane and associated with O(b) – Si – O(b)
252 bending was calculated at 434 cm^{-1} , whereas two overlapping modes at 450 cm^{-1} (1/4 of the intensity of
253 highest signal) and 454 cm^{-1} (1/2 of the intensity of highest signal) showed similar Mg-centred motions
254 together with O(b) – Si – O(a) bending. At 472 cm^{-1} , collective O – Mg – O bending modes in both the
255 TOT and O' layers were calculated, whereas two very weak signals at 476 and 479 cm^{-1} , hidden below
256 the previous one, were mainly due to Mg motions in the brucite-like layer. MgO_6 stretching modes in
257 association with O(b) – Si – O(a) bending in the TOT layer were calculated at 502 cm^{-1} (medium
258 intensity, 1/4 of the highest signal) and 527 cm^{-1} (medium to low intensity, 1/7 of the highest signal).

259 Making a comparison with the experimental results by Gopal et al. (2004), it is interesting to note that
260 this region presents a single, strong signal centred between $435 - 450\text{ cm}^{-1}$, with many shoulders and
261 small sub-peaks, which are overall in good agreement with the present theoretical simulation. The small
262 discrepancies are mainly due to the aluminium substitutions in both the TOT layer ($\text{Al}^{3+}/\text{Si}^{4+}$
263 substitutions) and the O' layer ($\text{Al}^{3+}/\text{Mg}^{2+}$ substitutions) that are a common feature of real samples and
264 also affects the mineral structure (Gopal et al., 2004; Valdrè et al., 2009; Moro et al., 2016; Moro et al.,
265 2019a; Moro et al., 2019b). The different crystal-chemistry not only affects, for example, the unit cell

266 structure (*e.g.* the larger **c**-axis parameter in Table 1) or the elastic properties of the mineral (Ulian et al.,
267 2018), but also the chemical environment of the anionic/cationic groups, and IR/Raman spectroscopies
268 are very sensitive to these variations. Also, it is important to stress that in the low-frequency region the
269 modes are expected to be affected by an extremely limited anharmonicity, probably smaller than 3–4 cm⁻¹,
270 ¹, as also discussed by Prencipe et al. (2009) for lizardite.

271

272 **3.2. The 500–1100 cm⁻¹ region**

273 The theoretical analysis revealed 33 optical modes in this region, whereas few and very broad peaks
274 were experimentally observed in both IR and Raman spectroscopies. Gopal et al. (2004) reported an
275 infrared signal at 653 cm⁻¹ that was assigned to M – OH libration. The same signal calculated at the
276 B3LYP-D* level is at 758 cm⁻¹, given by two modes at 753 and 758 cm⁻¹. This high discrepancy is due
277 to the anharmonic behaviour of this kind of modes for which the CRYSTAL code does not provide a
278 correction. Indeed, while the O – H stretching modes are usually uncoupled with other vibrational modes
279 and a reliable correction for anharmonicity was implemented in CRYSTAL by Tosoni et al. (2005), in
280 the case of H-bending modes such a correction is not applicable due to the coupling with other modes
281 having similar frequencies (Prencipe et al., 2009). Very recently, a computational approach based on the
282 vibrational configuration interaction method was proposed by Erba and co-workers (Erba et al., 2019a;
283 Erba et al., 2019b) to explicitly calculate the phonon-phonon coupling and evaluate the anharmonic
284 vibrational states of solids. However, this method is not available in version of the CRYSTAL code here
285 employed and, in addition, would demand high computational requirements for complex phases such as
286 layered silicates (Erba et al., 2019a; Erba et al., 2019b).

287 The present Density Functional Theory simulations provided also two very small IR peaks at 615 and
288 628 cm⁻¹ that were attributed to OH librations in the brucite-like layer. Given the previous consideration,

289 these signals are affected by anharmonicity and their position in real spectra should be considered with
290 care.

291 An asymmetric SiO_4 umbrella bending was calculated at 709 cm^{-1} in the infrared spectrum, but this
292 mode has an extremely low intensity and it could not be observable by experimental equipment or could
293 appear as a shoulder on the OH libration band. The symmetric counterpart, which is Raman active, was
294 calculated at 688 cm^{-1} , and it is the signal with highest intensity in the $0 - 1100\text{ cm}^{-1}$ spectral region.

295 The asymmetric Si – O(a) and Si – O(b) stretching modes were calculated at 989 (one mode) and 1013
296 cm^{-1} (two modes) in the infrared spectrum, which are in good agreement with the experimentally
297 measured values of 958 and 998 cm^{-1} reported by Gopal et al. (2004). Another Si – O(b) stretching mode
298 was calculated at 1092 cm^{-1} , appearing as a shoulder of the more intense Si – O(b) vibration. The Raman
299 spectrum contained the symmetric Si – O modes, with two Si – O(b) vibrations overlapping at about
300 1015 cm^{-1} and one Si – O(a) stretching mode at 1060 cm^{-1} . At 906 cm^{-1} an asymmetric Si – O(a) was
301 calculated in the Raman spectrum, but it presented almost zero intensity (1/5000 of the most intense
302 peak).

303

304

Table 4. Calculated isotopic shifts (cm^{-1}) according to the $^{25}\text{Mg} \rightarrow ^{24}\text{Mg}$ and $^{29}\text{Si} \rightarrow ^{28}\text{Si}$ substitutions (see paragraph 3 for details).

ν (cm^{-1})	IRRE P	Isotopic shift					ν (cm^{-1})	IRRE P	Isotopic shift				
		<i>Mg1</i>	<i>Mg2</i>	<i>Mg3</i>	<i>Mg4</i>	<i>Si</i>			<i>Mg1</i>	<i>Mg2</i>	<i>Mg3</i>	<i>Mg4</i>	<i>Si</i>
22	B _u	0.0	0.0	-0.1	0.0	0.0	431	B _u	0.0	-1.5	0.0	0.0	-0.2
25	A _u	0.0	0.0	-0.1	0.0	0.0	443	B _g	0.0	-3.1	0.0	0.0	-1.5
82	B _u	0.0	-0.1	-0.3	-0.1	-0.1	448	A _g	0.0	-3.6	0.0	0.0	-0.8
106	B _u	0.0	0.0	0.0	0.0	0.0	450	A _u	-1.7	-2.7	0.0	0.0	-1.4
106	A _g	0.0	0.0	0.0	0.0	0.0	454	B _u	-0.1	-0.6	0.0	0.0	-1.1
112	B _g	0.0	0.0	0.0	0.0	-0.9	458	B _g	0.0	0.0	-0.1	0.0	0.0
114	A _g	0.0	0.0	0.0	0.0	-0.9	458	A _g	0.0	-0.1	-0.1	0.0	-0.1
158	B _u	0.0	0.0	-0.7	-1.4	0.0	460	B _g	0.0	-2.6	0.0	0.0	-1.1
159	B _g	0.0	0.0	-2.1	0.0	0.0	472	A _u	-0.9	-0.1	-0.1	-0.3	-1.1
179	B _u	-0.5	-0.8	0.0	0.0	-0.5	476	A _g	0.0	0.0	-5.1	0.0	0.0
185	A _u	-0.4	-0.9	0.0	0.0	-0.5	476	B _u	0.0	0.0	-1.8	-3.4	0.0
200	A _g	0.0	0.0	0.0	0.0	-1.4	479	B _g	0.0	0.0	-5.2	0.0	0.0
245	B _g	-1.5	-2.4	0.0	0.0	-0.3	479	A _u	0.0	0.0	-1.6	-3.3	0.0
245	B _u	0.0	-0.5	0.0	0.0	-0.3	481	A _g	0.0	-1.4	0.0	0.0	-0.4
273	B _u	-0.3	-1.2	0.0	0.0	-0.4	483	A _g	0.0	0.0	-0.1	0.0	0.0
285	B _g	0.0	0.0	0.0	0.0	0.0	502	B _u	-1.5	-1.6	-0.3	-0.2	-0.1
287	A _g	0.0	0.0	0.0	0.0	0.0	519	B _g	0.0	-0.1	0.0	0.0	-0.3
294	A _g	0.0	0.0	0.0	0.0	-0.5	527	B _u	-0.5	-0.5	-0.2	-0.1	-0.2
298	A _u	-0.1	0.0	0.0	0.0	-0.4	529	A _u	0.0	0.0	0.0	0.0	-0.1
306	B _u	-0.2	0.0	-0.1	-0.1	0.0	531	A _g	0.0	-0.1	0.0	0.0	-0.1
307	B _g	0.0	-1.1	-0.1	0.0	-0.1	615	B _u	-0.2	-0.5	-1.3	-0.5	-0.1
312	A _u	0.0	-0.1	0.0	-0.1	-0.4	619	A _g	0.0	0.0	0.0	0.0	0.0
313	A _g	0.0	0.0	-0.2	0.0	-0.1	628	B _u	-0.1	-0.3	-3.2	-1.8	-0.1
314	B _g	0.0	-0.4	-0.1	0.0	-0.3	629	A _u	0.0	0.0	0.0	0.0	-0.3
329	B _u	-2.1	-0.7	0.0	0.0	-0.3	630	A _g	0.0	0.0	0.0	0.0	-0.3
334	A _g	0.0	0.0	0.0	0.0	-0.1	631	B _u	0.0	0.0	-0.1	-0.5	-0.3
340	B _g	0.0	-1.4	0.0	0.0	-0.5	631	B _g	0.0	0.0	-0.7	0.0	-0.2
353	A _u	-2.0	-0.5	0.0	-0.1	-2.6	635	B _g	0.0	0.0	-0.4	0.0	-0.2
355	B _g	0.0	-2.4	-0.1	0.0	-2.3	636	A _u	0.0	0.0	0.0	0.0	-0.2
375	A _g	0.0	-1.1	0.0	0.0	-0.2	688	A _g	0.0	0.0	0.0	0.0	-2.2
375	A _u	-0.2	-1.3	0.0	0.0	-0.8	709	B _u	-0.8	-1.5	-0.1	0.0	-2.7
377	B _u	-0.9	-0.8	0.0	-0.1	-0.7	753	B _u	-0.1	0.0	0.0	0.0	-1.1
387	A _g	0.0	-0.1	-3.3	0.0	0.0	758	A _u	0.0	0.0	0.0	0.0	-0.9
387	B _u	0.0	0.0	-1.1	-2.7	0.0	761	B _g	0.0	-0.2	0.0	0.0	-1.5
388	B _g	0.0	-0.9	-1.8	0.0	-0.8	763	A _g	0.0	0.0	0.0	0.0	-1.4
390	A _u	-0.1	0.0	-2.1	-2.0	0.0	796	A _g	0.0	0.0	0.0	0.0	-10.6
390	B _g	0.0	-0.1	-1.5	0.0	0.0	796	B _u	0.0	0.0	0.0	0.0	-11.0
392	A _g	0.0	-2.2	-0.1	0.0	-0.7	797	A _u	0.0	0.0	0.0	0.0	-11.2
397	A _u	0.0	0.0	-1.6	-1.5	0.0	798	B _g	0.0	-0.1	0.0	0.0	-10.6
398	B _u	0.0	-1.3	-2.1	-1.2	0.0	906	B _g	0.0	0.0	0.0	0.0	-4.1
400	B _u	-1.8	-1.8	0.0	0.0	-0.1	907	A _u	0.0	0.0	0.0	0.0	-4.1
400	A _u	-0.7	-0.5	0.0	0.0	-0.4	989	B _u	0.0	-0.1	-0.1	-0.1	-6.5
403	B _g	0.0	0.0	-2.3	0.0	0.0	1013	A _u	0.0	0.0	0.0	0.0	-4.6
407	B _u	0.0	0.0	-1.6	-1.5	0.0	1013	B _g	0.0	0.0	0.0	0.0	-4.6
412	A _u	0.0	0.0	-0.6	-0.2	0.0	1013	B _u	0.0	0.0	0.0	0.0	-4.6
415	A _g	0.0	0.0	0.0	0.0	0.0	1013	A _g	0.0	0.0	0.0	0.0	-4.6
426	B _u	-0.2	0.0	-0.2	-0.1	0.0	1060	A _g	0.0	0.0	0.0	0.0	-7.6
434	A _u	-4.7	0.0	-0.1	-0.1	0.0	1092	B _g	0.0	0.0	0.0	0.0	-1.6

Table 5. Calculated isotopic shifts (cm⁻¹) according to the ²D → ¹H substitutions (see paragraph 3 for details).

ν (cm ⁻¹)	IRREP	Isotopic shift			ν (cm ⁻¹)	IRREP	Isotopic shift		
		H1	H2	H3			H1	H2	H3
0	B _u	0.0	0.0	0.0	450	A _u	-4.3	-0.3	-1.7
0	B _u	0.0	0.0	0.0	454	B _u	-13.9	0.0	-0.6
0	A _u	0.0	0.0	0.0	458	B _g	-3.2	-14.1	-14.7
22	B _u	0.0	-0.1	-0.1	458	A _g	-0.2	-10.0	-10.0
25	A _u	0.0	0.0	-0.1	460	B _g	-2.6	0.0	-3.2
82	B _u	-0.1	-0.3	-0.6	472	A _u	-14.1	-0.4	-4.4
106	B _u	0.0	0.0	0.0	476	A _g	-9.5	-3.2	-10.6
106	A _g	0.0	0.0	0.0	476	B _u	0.0	-2.4	-9.2
112	B _g	0.0	-0.1	0.0	479	B _g	0.0	-1.6	-7.4
114	A _g	0.0	0.0	0.0	479	A _u	-0.1	-0.1	-5.0
158	B _u	0.0	-6.4	-8.9	481	A _g	-5.0	-2.0	-5.7
159	B _g	0.0	-3.9	-11.3	483	A _g	0.0	-2.2	-2.2
179	B _u	-1.0	0.0	0.0	502	B _u	-2.6	-0.1	-5.8
185	A _u	-0.3	0.0	-0.1	519	B _g	-1.0	-0.4	-15.7
200	A _g	-0.2	0.0	0.0	527	B _u	-2.7	-0.8	-22.9
245	B _g	-2.6	-0.1	-0.1	529	A _u	-0.2	0.0	-29.5
245	B _u	-1.4	0.0	-0.3	531	A _g	-0.7	-0.1	-35.8
273	B _u	-5.0	0.0	0.0	615	B _u	-38.4	-52.9	-86.8
285	B _g	0.0	-0.3	-0.3	619	A _g	-41.5	-53.1	-87.8
287	A _g	0.0	-1.0	-0.1	628	B _u	-13.7	-7.9	-41.5
294	A _g	-0.9	-5.2	-3.0	629	A _u	-54.2	-86.7	-100.5
298	A _u	-0.2	-1.7	-12.8	630	A _g	-11.1	-4.4	-45.6
306	B _u	-0.2	-8.6	-15.8	631	B _u	-3.3	-2.5	-10.0
307	B _g	-3.3	-3.7	-11.4	631	B _g	-49.7	-76.3	-111.8
312	A _u	-0.1	-5.2	-7.2	635	B _g	-3.1	0.0	-24.5
313	A _g	-0.6	-6.1	-10.5	636	A _u	-5.7	-0.1	-31.9
314	B _g	-1.6	-2.1	-3.8	688	A _g	-56.5	-0.2	-0.2
329	B _u	-2.7	-1.6	-0.3	709	B _u	-76.8	-0.2	-0.4
334	A _g	-2.4	-0.2	-0.5	753	B _u	-44.6	-0.2	-0.5
340	B _g	-0.1	0.0	-1.6	758	A _u	-122.4	-0.1	-0.4
353	A _u	0.0	-3.2	-36.1	761	B _g	-125.8	-0.2	-0.4
355	B _g	0.0	-1.2	-8.1	763	A _g	-75.1	-0.3	-0.5
375	A _g	-7.1	-20.6	-23.5	796	A _g	-2.3	-1.1	-1.5
375	A _u	-2.3	-15.4	-24.1	796	B _u	-2.3	-0.9	-1.4
377	B _u	-1.9	-25.9	-45.9	797	A _u	-1.7	-0.9	-1.9
387	A _g	-0.1	-11.9	-14.7	798	B _g	-2.7	-0.6	-1.8
387	B _u	0.0	-10.2	-10.3	906	B _g	-0.5	-0.1	-0.3
388	B _g	-0.3	-11.5	-32.9	907	A _u	-0.5	-0.1	-0.3
390	A _u	0.0	-14.3	-16.8	989	B _u	-0.1	-0.2	-0.4
390	B _g	0.0	-1.4	-7.5	1013	A _u	-0.1	0.0	0.0
392	A _g	-0.7	-2.8	-15.5	1013	B _g	-0.1	0.0	0.0
397	A _u	-1.5	-6.7	-14.3	1013	B _u	-0.1	0.0	0.0
398	B _u	-1.2	-10.9	-17.5	1013	A _g	-0.1	0.0	0.0
400	B _u	-1.8	0.0	-0.3	1060	A _g	-0.2	0.0	0.0
400	A _u	-3.5	0.0	0.0	1092	B _g	0.0	-0.1	-0.1
403	B _g	0.0	-2.6	-14.6	1092	A _u	0.0	-0.1	-0.1
407	B _u	0.0	-0.1	-6.3	3849	B _u	-1037.0	0.0	0.0
412	A _u	0.0	-7.2	-9.5	3850	A _g	-1036.4	0.0	0.0
415	A _g	0.0	-21.3	-22.3	3975	B _g	0.0	0.0	-1074.9
426	B _u	0.0	-17.7	-18.8	3975	A _u	0.0	0.0	-1074.9
434	A _u	-0.1	-17.7	-20.5	3976	B _u	0.0	-1072.5	4.7
431	B _u	-0.7	-0.2	-0.1	3976	A _g	0.0	-1071.7	5.0
443	B _g	-12.3	-37.4	-38.7	3987	B _u	0.0	-4.7	-1082.8
448	A _g	-11.0	-19.3	-44.6	3988	A _g	0.0	-4.9	-1081.9

3.3. The 3700–4000 cm⁻¹ region.

This is the region dominated by the hydroxyl stretching modes of both the talc-like and the brucite-like layer. Here, 8 optical modes were computed, four IR-active ($A_u + 3B_u$) and four active in Raman spectroscopy ($3A_g + B_g$). Within the harmonic approximation, the calculated vibrational frequency of the infrared OH-modes were 3849 cm⁻¹, 3975 cm⁻¹, 3976 cm⁻¹ and 3987 cm⁻¹, whereas the frequencies of Raman-active modes were 3850 cm⁻¹, 3975 cm⁻¹, 3976 cm⁻¹ and 3988 cm⁻¹. As reported in Table 2, the anharmonic constant for these modes is quite remarkable, of about 150 cm⁻¹, in agreement with previous theoretical observations (Tosoni et al., 2005; Prencipe et al., 2009). This is a well-known issue related to the very low mass of hydrogen, whose vibrational displacement is often large, whereas the assumption of harmonic oscillators requires small nuclear movements. For this means, the correction proposed by Tosoni and co-workers (2005), which is based on a numerical solution of the Schrödinger equation along the O – H coordinate for fully decoupled hydroxyl stretching modes, was employed. The interested readers can find further details in the work of Tosoni et al. (2005).

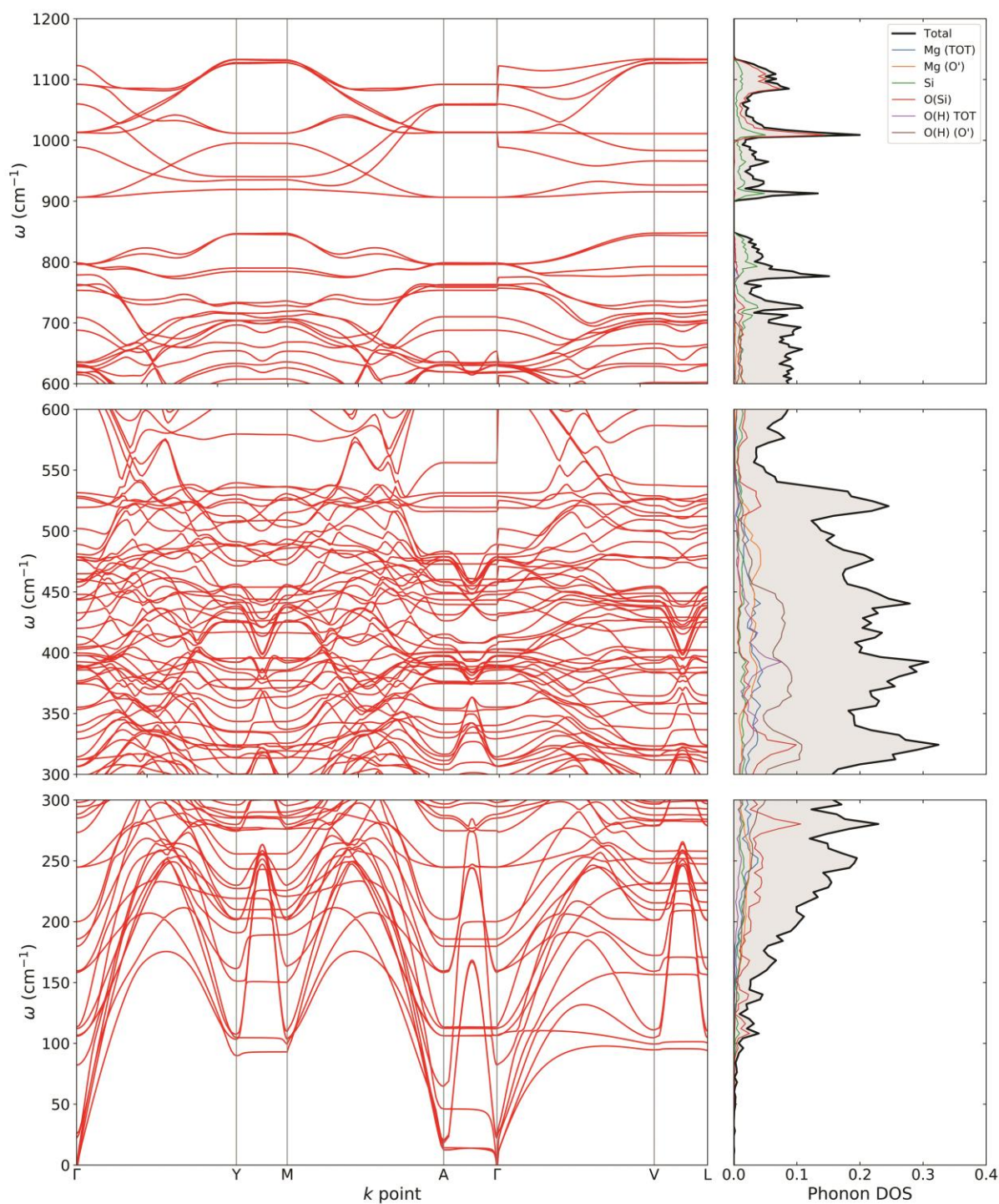
By considering the anharmonic vibrational frequencies, the first two lines (101, B_u and 102, A_g) reported in Table 2, centred at about 3700 cm⁻¹, were related to OH stretching modes of the TOT layer, whereas the other six vibrations at higher frequencies (3830 – 3850 cm⁻¹) are due to O – H vibrations in the O' layer. These figures are quite different from those experimentally measured by Gopal et al. (2004), who reported these signals between 3438 cm⁻¹ and 3678 cm⁻¹, and can be explained by the different crystal-chemistry of the O' and TOT layers, which commonly present Al³⁺/Mg²⁺ and Al³⁺/Si⁴⁺ substitutions, respectively.

3.4. Phonon dispersion relations.

Phonon dispersion calculations were performed by sampling other \mathbf{k} -points in the first Brillouin Zone other than Γ ($\mathbf{k} = 0$) using a direct-space approach (Dove, 1993; Parlinski et al., 1997; Wallace, 1998). The phonon sampling was conducted on a clinoclone $2 \times 2 \times 2$ supercell constructed from the primitive cell of the mineral.

Phonon dispersion curves of monoclinic clinoclone in the path $\Gamma \rightarrow Y \rightarrow M \rightarrow A \rightarrow \Gamma \rightarrow Y \rightarrow V \rightarrow L \rightarrow \Gamma$ is reported in Figure 3 for the $0 - 1200 \text{ cm}^{-1}$ range, alongside the calculated total and atom-projected phonon density of states (DOS). The low-frequency region ($\nu < 550 \text{ cm}^{-1}$) is characterized by magnesium and oxygen vibrations, whereas at higher wavenumbers ($750 \text{ cm}^{-1} < \nu < 1200 \text{ cm}^{-1}$) the phonon dispersion is completely dominated by Si – O phonon modes. The spectral region between 550 cm^{-1} and 750 cm^{-1} shows a small contribution from Mg, Si and O atoms to the total DOS, which is mainly due to vibrational motion of hydrogen atoms (projection not showed in the figure for the sake of clarity). As previously discussed, there is a strong anharmonic component in these phonon modes that are not calculated by the CRYSTAL code at the moment. For this reason, this portion of the phonon spectrum has to be considered subject to possible shifts at different wavenumbers.

Acoustic phonon dispersion curves are in adequate agreement with those experimentally measured by inelastic neutron scattering technique by Collins et al. (1993), albeit the poor resolution of the phonon spectra made the comparison difficult.



347

348 **Figure 3.** DFT/B3LYP-D* phonon dispersion relations and phonon density of states (DOS) of
 349 monoclinic clinocllore (space group $C2/m$) in the frequency range 0 – 1200 cm^{-1} .

350 As a final note on the phonon properties (Γ -point frequencies and phonon dispersion relations), the
351 authors are aware that clinocllore is typically found with $\text{Al}^{3+}/\text{Si}^{4+}$ substitutions in both the TOT layer
352 and O' sheet, and other isomorphic substitution may occur in the mineral structure. In general, as reported
353 by several authors (Pawley and Jones, 2011; Ulian et al., 2014; Jollands et al., 2020), crystal-chemical
354 variations from stoichiometric structures can deeply affect the vibrational spectrum. Among the possible
355 effect, it is possible to cite:

356 (i) increasing number of IR/Raman signals due to lower symmetry of the system (*i.e.*, degeneracy loss
357 of some vibrational modes or activation of silent modes);

358 (ii) blue or red shifts of the peaks because of the different chemical environment around the vibrating
359 group and/or

360 (iii) more or less intense signals due to variations of the dipole moment (IR) or polarizability (Raman).

361 It is possible to extend these considerations to $\mathbf{k} \neq 0$, thus the phonon band structure is more complex
362 and elaborate in a cationic/anionic-substituted mineral phase than that of the end-member term.

363 However, it was decided to start with the vibrational analysis by considering the simplest clinocllore
364 system, which is the stoichiometric one, a necessary starting point to assign IR/Raman signals to specific
365 vibrations in the structure. Although the system is simple, it represents a novelty because to the authors'
366 knowledge no theoretical information on this subject is present in literature. In addition, Density
367 Functional Theory simulations involving isomorphic substitutions are very demanding from the
368 computational side, in particular for the phonon dispersion relations where supercells are required, and
369 the interpretation of the resulting phonon bands could be a daunting task without those from a reference
370 phase. A comparison between the present theoretical result for the stoichiometric clinocllore and those
371 presenting different kinds and degrees of isomorphic substitutions will be the subject of future works,

372 which will also aid the assignment of experimental IR/Raman signals to specific vibrational modes in
373 the structure.

374

375 **4. Conclusions**

376 In this theoretical work, a detailed and accurate analysis of the vibrational properties of monoclinic
377 clinochlore was carried out by means of Density Functional Theory simulations. The results were
378 extensively presented and discussed against the few available experimental findings, with a general good
379 agreement on both the pattern (peak positions and intensities in the IR/Raman spectra) and assignment
380 of the normal modes. The theoretical approach provided further details and extended the knowledge on
381 the vibrational features of this mineral phase, which can be exploited in future studies involving the bulk
382 and the surface of clinochlore.

383 The small differences between the calculated results and the experimental data in literature are mainly
384 due to the crystal-chemistry of the simulated model. In fact, it was considered an ideal, completely
385 magnesian monoclinic clinochlore without any of the typical substitutions occurring in this mineral, *e.g.*
386 $\text{Al}^{3+}/\text{Si}^{4+}$ or $\text{Al}^{3+}/\text{Mg}^{2+}$ in the tetrahedral and O' sites, respectively.

387 As a final note, the present results showed the relevance of anharmonic OH-modes in both infrared
388 and Raman spectra. While an anharmonic correction was employed in this work for the characterization
389 of the hydroxyl stretching region, at the moment the CRYSTAL code does not calculate the anharmonic
390 contribution for the Mg – O – H (libration) modes.

391

392

393

394 **Acknowledgments**

395 This work is dedicated to the memory of Professor Emilio Galan, who was a world-known scientist, a
396 stimulating collaborator of many works, and a sincere good friend.

397

398

399 **Bibliographic references**

400 Balan, E., Saitta, A.M., Mauri, F., Calas, G., 2001. First-principles modeling of the infrared spectrum
401 of kaolinite. *Am. Mineral.* 86, 1321-1330.

402 Bayliss, P., 1975. Nomenclature of the trioctahedral chlorites. *Can. Mineral.* 13, 178-180.

403 Becke, A.D., 1993. A New Mixing of Hartree-Fock and Local Density-Functional Theories. *J. Chem.*
404 *Phys.* 98, 1372-1377, 10.1063/1.464304.

405 Bhattacharai, A., El-Khoury, P.Z., 2019. Nanoscale Chemical Reaction Imaging at the Solid-Liquid
406 Interface via TERS. *J. Phys. Chem. Lett.* 10, 2817-2822, 10.1021/acs.jpcclett.9b00935.

407 Civalleri, B., Zicovich-Wilson, C.M., Valenzano, L., Ugliengo, P., 2008. B3LYP augmented with an
408 empirical dispersion term (B3LYP-D*) as applied to molecular crystals. *CrystEngComm* 10, 405-410,
409 10.1039/b715018k.

410 Collins, D.R., Stirling, W.G., Catlow, C.R.A., Rowbotham, G., 1993. Determination of acoustic
411 phonon dispersion curves in layer silicates by inelastic neutron scattering and computer simulation
412 techniques. *Phys. Chem. Miner.* 19, 520-527, 10.1007/BF00203052.

413 Dominguez, G., Mcleod, A.S., Gainsforth, Z., Kelly, P., Bechtel, H.A., Keilmann, F., Westphal, A.,
414 Thiemens, M., Basov, D.N., 2014. Nanoscale infrared spectroscopy as a non-destructive probe of
415 extraterrestrial samples. *Nat. Commun.* 5, 5445, 10.1038/Ncomms6445.

416 Dove, M.T., 1993. *Introduction to Lattice Dynamics*. Cambridge University Press.

417 Dovesi, R., Erba, A., Orlando, R., Zicovich-Wilson, C.M., Civalleri, B., Maschio, L., Rerat, M.,
 418 Casassa, S., Baima, J., Salustro, S., Kirtman, B., 2018. Quantum-mechanical condensed matter
 419 simulations with CRYSTAL. *Wires Comput Mol Sci* 8, E1360, 10.1002/Wcms.1360.

420 Erba, A., Maul, J., Ferrabone, M., Carbonniere, P., Rerat, M., Dovesi, R., 2019a. Anharmonic
 421 Vibrational States of Solids from DFT Calculations. Part I: Description of the Potential Energy Surface.
 422 *J. Chem. Theory Comput.* 15, 3755-3765, 10.1021/acs.jctc.9b00293.

423 Erba, A., Maul, J., Ferrabone, M., Dovesi, R., Rerat, M., Carbonniere, P., 2019b. Anharmonic
 424 Vibrational States of Solids from DFT Calculations. Part II: Implementation of the VSCF and VCI
 425 Methods. *J. Chem. Theory Comput.* 15, 3766-3777, 10.1021/acs.jctc.9b00294.

426 Ferrero, M., Rerat, M., Kirtman, B., Dovesi, R., 2008a. Calculation of first and second static
 427 hyperpolarizabilities of one- to three-dimensional periodic compounds. Implementation in the
 428 CRYSTAL code. *J. Chem. Phys.* 129, 244110, 10.1063/1.3043366.

429 Ferrero, M., Rerat, M., Orlando, R., Dovesi, R., 2008b. The calculation of static polarizabilities of 1-
 430 3D periodic compounds. The implementation in the CRYSTAL code. *J. Comput. Chem.* 29, 1450-1459,
 431 10.1002/jcc.20905.

432 Firkala, T., Kuschewski, F., Norenberg, T., Klopff, J.M., Pashkin, A., Foerstendorf, H., Rudolph, M.,
 433 Kehr, S.C., Eng, L.M., 2018. Near-Field Optical Examination of Potassium n-Butyl
 434 Xanthate/Chalcopyrite Flotation Products. *Minerals-Basel* 8, 12, 10.3390/min8030118.

435 Fries, M., Steele, A., 2018. Raman spectroscopy and confocal raman imaging in mineralogy and
 436 petrography, Springer Ser. Surf. Sci. Springer Verlag, pp. 209-236.

437 Gatti, C., Saunders, V.R., Roetti, C., 1994. Crystal-field effects on the topological properties of the
 438 electron-density in molecular-crystals - the case of urea. *J. Chem. Phys.* 101, 10686-10696,
 439 10.1063/1.467882.

440 Gopal, N.O., Narasimhulu, K.V., Rao, J.L., 2004. Optical absorption, EPR, infrared and Raman
 441 spectral studies of clinocllore mineral. *J. Phys. Chem. Solids* 65, 1887-1893,
 442 10.1016/j.jpcs.2004.07.003.

443 Grimme, S., 2006. Semiempirical GGA-type density functional constructed with a long-range
 444 dispersion correction. *J. Comput. Chem.* 27, 1787-1799, 10.1002/jcc.20495.

445 Jollands, M.C., Blanchard, M., Balan, E., 2020. Structure and theoretical infrared spectra of OH defects
 446 in quartz. *Eur. J. Mineral.* 32, 311-323, 10.5194/ejm-32-311-2020.

447 King, H.E., Geisler, T., 2018. Tracing mineral reactions using confocal raman spectroscopy. *Minerals-*
 448 *Basel* 8, 10.3390/min8040158.

449 Kroumova, E., Aroyo, M.I., Perez-Mato, J.M., Kirov, A., Capillas, C., Ivantchev, S., Wondratschek,
 450 H., 2003. Bilbao crystallographic server: Useful databases and tools for phase-transition studies. *Phase*
 451 *Transitions* 76, 155-170, 10.1080/0141159031000076110.

452 Kumar, N., Wondergem, C.S., Wain, A.J., Weckhuysen, B.M., 2019. In Situ Nanoscale Investigation
 453 of Catalytic Reactions in the Liquid Phase Using Zirconia-Protected Tip-Enhanced Raman Spectroscopy
 454 Probes. *J. Phys. Chem. Lett.* 10, 1669-1675, 10.1021/acs.jpcllett.8b02496.

455 Lafuente, B., Downs, R.T., Yang, H., Stone, N., 2016. The power of databases: The RRUFF project,
 456 Highlights in Mineralogical Crystallography. Walter de Gruyter GmbH, Berling, Germany, pp. 1-29.

457 Lee, C.T., Yang, W.T., Parr, R.G., 1988. Development of the Colle-Salvetti Correlation-Energy
 458 Formula into a Functional of the Electron-Density. *Phys. Rev. B* 37, 785-789,
 459 10.1103/PhysRevB.37.785.

460 Maschio, L., Kirtman, B., Orlando, R., Rerat, M., 2012. Ab initio analytical infrared intensities for
 461 periodic systems through a coupled perturbed Hartree-Fock/Kohn-Sham method. *J. Chem. Phys.* 137,
 462 204113, 10.1063/1.4767438.

463 Maschio, L., Kirtman, B., Rerat, M., Orlando, R., Dovesi, R., 2013a. Ab initio analytical Raman
464 intensities for periodic systems through a coupled perturbed Hartree-Fock/Kohn-Sham method in an
465 atomic orbital basis. I. Theory. J. Chem. Phys. 139, 164101, 10.1063/1.4824442.

466 Maschio, L., Kirtman, B., Rerat, M., Orlando, R., Dovesi, R., 2013b. Ab initio analytical Raman
467 intensities for periodic systems through a coupled perturbed Hartree-Fock/Kohn-Sham method in an
468 atomic orbital basis. II. Validation and comparison with experiments. J. Chem. Phys. 139, 164102,
469 10.1063/1.4824443.

470 Momma, K., Izumi, F., 2011. VESTA 3 for three-dimensional visualization of crystal, volumetric and
471 morphology data. J. Appl. Crystallogr. 44, 1272-1276, 10.1107/s0021889811038970.

472 Monkhorst, H.J., Pack, J.D., 1976. Special points for Brillouin-zone integrations. Phys. Rev. B 8, 5188-
473 5192.

474 Moro, D., Ulian, G., Valdrè, G., 2019a. 3D meso-nanostructures in cleaved and nanolithographed Mg-
475 Al-hydroxysilicate (clinochlore): Topology, crystal-chemistry, and surface properties. Appl. Clay Sci.
476 169, 74-80, 10.1016/j.clay.2018.12.020.

477 Moro, D., Ulian, G., Valdrè, G., 2015. Single molecule investigation of glycine-chlorite interaction by
478 cross-correlated scanning probe microscopy and quantum mechanics simulations. Langmuir 31, 4453-
479 4463, 10.1021/acs.langmuir.5b00161.

480 Moro, D., Ulian, G., Valdrè, G., 2016. Nanoscale cross-correlated AFM, Kelvin probe, elastic modulus
481 and quantum mechanics investigation of clay mineral surfaces: The case of chlorite. Appl. Clay Sci. 131,
482 175-181, 10.1016/j.clay.2015.11.023.

483 Moro, D., Ulian, G., Valdrè, G., 2019b. Amino acids-clay interaction at the nano-atomic scale: The L-
484 alanine-chlorite system. Appl. Clay Sci. 172, 28-39, 10.1016/j.clay.2019.02.013.

485 Nada, R., Nicholas, J.B., McCarthy, M.I., Hess, A.C., 1996. Basis sets for ab initio periodic Hartree-
 486 Fock studies of zeolite/adsorbate interactions: He, Ne, and Ar in silica sodalite. *Int. J. Quantum Chem.*
 487 60, 809-820, 10.1002/(sici)1097-461x(1996)60:4<809::aid-qua3>3.0.co;2-0.
 488 Parlinski, K., Li, Z.Q., Kawazoe, Y., 1997. First-principles determination of the soft mode in cubic
 489 ZrO₂. *Phys. Rev. Lett.* 78, 4063-4066, DOI 10.1103/PhysRevLett.78.4063.
 490 Pascale, F., Zicovich-Wilson, C.M., Gejo, F.L., Civalleri, B., Orlando, R., Dovesi, R., 2004. The
 491 calculation of the vibrational frequencies of crystalline compounds and its implementation in the
 492 CRYSTAL code. *J. Comput. Chem.* 25, 888-897, Doi 10.1002/Jcc.20019.
 493 Pascale, F., Zicovich-Wilson, C.M., Orlando, R., Roetti, C., Ugliengo, P., Dovesi, R., 2005. Vibration
 494 frequencies of Mg₃Al₂Si₃O₁₂ pyrope. An ab initio study with the CRYSTAL code. *J. Phys. Chem. B* 109,
 495 6146-6152, 10.1021/jp050316z.
 496 Pawley, A.R., Jones, R.L., 2011. Hydroxyl stretching in phyllosilicates at high pressures and
 497 temperatures: An infrared spectroscopic study. *Phys. Chem. Miner.* 38, 753-765, 10.1007/s00269-011-
 498 0448-x.
 499 Phuakkong, O., Bobuatong, K., Pantu, P., Boekfa, B., Probst, M., Limtrakul, J., 2011. Glycine Peptide
 500 Bond Formation Catalyzed by Faujasite. *ChemPhysChem* 12, 2160-2168, 10.1002/cphc.201100047.
 501 Prencipe, M., Noel, Y., Bruno, M., Dovesi, R., 2009. The vibrational spectrum of lizardite-1T
 502 [Mg(3)Si(2)O(5)(OH)(4)] at the Gamma point: A contribution from an ab initio periodic B3LYP
 503 calculation. *Am. Mineral.* 94, 986-994.
 504 Prencipe, M., Pascale, F., Zicovich-Wilson, C.M., Saunders, V.R., Orlando, R., Dovesi, R., 2004. The
 505 vibrational spectrum of calcite (CaCO₃): an ab initio quantum-mechanical calculation. *Phys. Chem.*
 506 *Miner.* 31, 559-564, DOI 10.1007/s00269-004-0418-7.

507 Rinaudo, C., Roz, M., Boero, V., Franchini-Angela, M., 2004. FT-Raman spectroscopy on several di-
 508 and tri-octahedral T-O-T phyllosilicates. *Neues Jb Miner Monat*, 537-554, 10.1127/0028-
 509 3649/2004/2004-0537.

510 Rosso, K.M., Bodnar, R.J., 1995. Microthermometric and Raman-spectroscopic detection limits of
 511 CO₂ in fluid inclusions and the Raman-spectroscopic characterization of CO₂. *Geochim. Cosmochim.*
 512 *Acta* 59, 3961-3975, Doi 10.1016/0016-7037(95)94441-H.

513 Stueckenschneider, K., Merz, J., Schembecker, G., 2014. Molecular Interaction of Amino Acids with
 514 Acidic Zeolite BEA: The Effect of Water. *J. Phys. Chem. C* 118, 5810-5819, 10.1021/jp411734j.

515 Tosoni, S., Pascale, F., Ugliengo, P., Orlando, R., Saunders, V.R., Dovesi, R., 2005. Quantum
 516 mechanical calculation of the OH vibrational frequency in crystalline solids. *Mol. Phys.* 103, 2549-2558,
 517 10.1080/00268970500180808.

518 Ugliengo, P., Viterbo, D., Chiari, G., 1993. MOLDRAW: molecular graphic on a personal computer.
 519 *Z. Kristallogr.* 207, 9-23, 10.1524/zkri.1993.207.Part-1.9.

520 Ulian, G., Moro, D., Valdrè, G., 2016. First-principles study of structural and surface properties of
 521 (001) and (010) surfaces of hydroxylapatite and carbonated hydroxylapatite. *J. Appl. Crystallogr.* 49,
 522 1893–1903, 10.1107/S160057671601390X.

523 Ulian, G., Moro, D., Valdrè, G., 2018. First principle investigation of the mechanical properties of
 524 natural layered nanocomposite: Clinocllore as a model system for heterodesmic structures. *Composite*
 525 *Structures* 202, 551-558, 10.1016/j.compstruct.2018.02.089.

526 Ulian, G., Valdrè, G., 2015. Density functional investigation of the thermo-physical and thermo-
 527 chemical properties of 2M(1) muscovite. *Am. Mineral.* 100, 935-944, 10.2138/am-2015-5086.

528 Ulian, G., Valdrè, G., Corno, M., Ugliengo, P., 2014. DFT investigation of structural and vibrational
 529 properties of type B and mixed A-B carbonated hydroxylapatite. *Am. Mineral.* 99, 117-127,
 530 10.2138/am.2014.4542.

531 Valdrè, G., 2007. Natural nanoscale surface potential of clinochlore and its ability to align nucleotides
 532 and drive DNA conformational change. *Eur. J. Mineral.* 19, 309-319, Doi 10.1127/0935-
 533 1221/2007/0019-1732.

534 Valdrè, G., Malferrari, D., Brigatti, M.F., 2009. Crystallographic Features and Cleavage
 535 Nanomorphology of Chlinochlore: Specific Applications. *Clays Clay Miner.* 57, 183-193,
 536 10.1346/Ccmn.2009.0570205.

537 Valdrè, G., Moro, D., Hounscome, C.M., Antognozzi, M., 2012. SPM nanolithography of hydroxy-
 538 silicates. *Nanotechnology* 23, 85301-85301, 10.1088/0957-4484/23/38/385301.

539 Valdrè, G., Moro, D., Ulian, G., 2011a. Interaction of organic molecules with layer silicates, oxides
 540 and hydroxides and related surface-nano-characterization techniques, in: Brigatti, M.F., Mottana, A.
 541 (Eds.), *Layered Mineral Structures and Their Application in Advanced Technologies*, pp. 313-334.

542 Valdrè, G., Moro, D., Ulian, G., 2011b. Nucleotides, RNA and DNA selective adsorption on atomic-
 543 flat Mg-Al-hydroxysilicate substrates. *Micro & Nano Letters* 6, 922-926, 10.1049/mnl.2011.0546.

544 Valdrè, G., Tosoni, S., Moro, D., 2011c. Zeolitic-type 'Bronsted-Lowry sites distribution imaged on
 545 clinochlore. *Am. Mineral.* 96, 1461-1466, 10.2138/am.2011.3774.

546 Valenzano, L., Torres, F.J., Klaus, D., Pascale, F., Zicovich-Wilson, C.M., Dovesi, R., 2006. Ab initio
 547 study of the vibrational spectrum and related properties of crystalline compounds; the case of CaCO₃
 548 calcite. *Z. Phys. Chem.* 220, 893-912, 10.1524/zpch.2006.220.7.893.

549 Wallace, D.W., 1998. *Thermodynamics of Crystals*. Dover Publications.

550 Welch, M.D., Marshall, W.G., 2001. High-pressure behavior of clinochlore. *Am. Mineral.* 86, 1380-
 551 1386.

552 Wiewiora, A., 1990. Crystallochemical Classifications of Phyllosilicates Based on the Unified System
 553 of Projection of Chemical-Composition .3. The Serpentine-Kaolin Group. *Clay Miner.* 25, 93-98, DOI
 554 10.1180/claymin.1990.025.1.10.